Edge-preserving denoising for intra-operative cone beam CT in endovascular aneurysm repair

Yi Liu, Miguel Castro, Mathieu Lederlin, Huazhong Shu, Adrien Kaladji, Pascal Haigron

Edge-preserving Denoising for Intra-operative Cone Beam CT in Endovascular Aneurysm Repair

Yi Liu[a,b,1], Miguel Castro[a,b], Mathieu Lederlin[a,b,c], Huazhong Shu[e,f], Adrien Kaladji[a,b,d], Pascal Haigron[a,b,e]

[a] INSERM, U1099, Rennes, F-35000, France
[b] Université de Rennes 1, LTSI, Rennes, F-35000, France
[c] CHU Rennes, Department of Radiology, F-35000, France
[d] CHU Rennes, Department of Cardiothoracic and Vascular Surgery, F-35000, France
[e] Ctr Rech Informat Med Sino Francais, CRIBs, Rennes, F-35000, France
[f] Southeast University, Laboratory of Image Science and Technology, Key Laboratory of Computer Network and Information Integration of Ministry of Education, Nanjing 210096, Jiangsu, Peoples R China

Corresponding author: Pascal Haigron

Email: Pascal.Haigron@univ-rennes1.fr

[1]Present address: National Key laboratory for Electronic Measurement Technology, North University of China, 030051, Tai Yuan, Peoples R China

Highlights

1, We propose a new edge-preserving penalty based PWLS (penalized weighted least-squares) algorithm for intra-operative CBCT with low dose radiation from the EVAR (Endovascular aneurysm repair) operation.

2, The proposed edge-preserving penalty absorbs the concept of bilateral filter and can not only suppress noise and artifacts in CBCT images, but also improve the contrast for low-contrast regions.

3, Experimental comparisons demonstrate that the proposed edge-preserving penalty outperforms the isotropic, anisotropic, TV and Huber penalties.

Abstract: C-arm cone-beam computed tomography (CBCT) acquisition during endovascular aneurysm repair (EVAR) is an emergent technology with more and more applications. It offers real time imaging with a stationary patient and provides 3-D information to achieve guidance of intervention. However, there is growing concern on the overall radiation doses delivered to patients all along the endovascular management due to pre-, intra-, and post-operative X-ray imaging. Manufactures may have their low dose protocols to realize reduction of radiation dose, but CBCT with a low dose protocol has too many artifacts, particularly streak artifacts, and decreased contrast-to-noise ratio (CNR). To reduce noise and artifacts, a penalized weighted least-squares (PWLS) algorithm with an edge-preserving penalty is proposed. The proposed method is evaluated by quantitative parameters including a defined signal-to-noise ratio (SNR), CNR, and modulation transfer function (MTF) on clinical CBCT. Comparisons with PWLS algorithms with isotropic, TV, Huber, anisotropic penalties demonstrate that the proposed edge-preserving penalty performs well not only on edge preservation, but also on streak artifacts suppression, which may be crucial for observing guidewire and stentgraft in EVAR.

Keywords: Endovascular aneurysm repair, intra-operative CBCT, image denoising, penalized weighted least-squares, edge-preserving penalty.

1. Introduction

CBCT (cone-beam computed tomography) mounted on a C-arm in the interventional radiology (IR) suite employing digital flat-panel detectors, has been an exciting technology with an advanced imaging capability of 3D acquisition. For clinicians, this kind of acquisition providing CT-like images is particularly useful for vessel catheterization and was described for the first time in cerebral aneurysm embolization[1]. The first application of 3D CBCT acquisition with contrast media injection in an EVAR (endovascular aneurysm repair) aimed to detect any potential complication (endoleaks, stentgraft kinking) that can be treated immediately after the procedure[2-5], i.e., after the deployment of the stentgraft. More recently, 3D CBCT acquisition (without contrast media injection) was described in order to fuse the preoperative CT-scan by means of a 3D/3D rigid bone registration[6-11]. With this fusion imaging technique, catheterization and stentgraft deployment can be achieved with a 3D visualization of the vascular tree and leads to a significant decrease of contrast media volume injection[6-11].

Even though CBCT mounted on a C-arm provides high quality fluoroscopy image and offers benefits for patients, there is growing concern on the overall radiation doses delivered to patients all along the endovascular management of their AAA (abdominal aorta aneurysm) due to pre-, intra-, and post-operative X-ray imaging[12]. Despite the radiation dose related to 3D CBCT acquisition, EVAR is one of the most irradiated procedures in vascular surgery, even more for complex repair such as fenestrated and branched endograft[13]. As a consequence, it is very important to reduce the radiation dose related to CBCT, not only for patient care, but also for the medical staff to avoid or reduce potential determinist and stochastic risks from radiological procedure[14-16]. One effective way to reduce the radiation dose is to choose a scanning protocol with less rotation time, which is already preset in the C-arm CBCT system. It is difficult in fact to control patient dose in some C-arm CBCT systems because C-arm CBCT operates with automatic exposure control systems through controlling the current intensity (mA), and if necessary, the voltage (kVp) to maintain the signal-to-noise ratio (SNR)[17]. In practice, different manufactures may have different low dose protocols to realize reduction of radiation dose. Actually, the noise in CBCT with low dose protocol is a tricky issue due to the low current intensity used and the wide collimation leading to increased scatter radiation, and subsequent artifacts, particularly streak artifacts, and decreased CNR (Contrast-to-Noise Ratio)[18]. Noise and artifact suppression for low dose CBCT is therefore crucial to access to the benefits of CBCT reconstruction images and subsequent image processing such as segmentation and registration.

Several techniques have been proposed to remove noise and artifacts in CT and CBCT. They are generally divided into three strategies: (1) Projection domain denoising, in which the projection data is seen as an image and processed by various sophisticated denoising algorithms. Thereby reconstructed images can be obtained from the denoised projections[19-21]. One distinct advantage is that this kind of technique takes noise properties in projection space into account while the potential disadvantage that the definition of edge in projection domain is not definite, resulting in sharpness loss in image domain, cannot be ignored. (2) Image domain denoising (post-processing), in which various filters can be directly applied on the finally reconstructed images. Many outstanding filters considering both noise suppression and edge preserving have been performed for CT denoising, such as nonlocal means filtering[22,23] and dictionary learning based filtering[24-26]. However, it is difficult to establish a noise model in the image domain due to the fact that the image noise always changes with scanning parameters. (3) Statistical iterative reconstruction (SIR), which consists in finding an optimal solution by maximizing or minimizing an objective function constructed according to the noise characteristics of the projections, has been demonstrated to be effective in removing noise and artifacts in both projection and image domain[27-31]. Although these algorithms yield excellent results with respect to noise and artifacts suppression, they are on a large extent not independent, requiring more detailed information such as scanning geometry, correction physics, etc.[22]. Its limitation appeals a more broadly used denoising method to perform on different systems. Although there are few reports for C-arm CBCT denoising in EVAR, some techniques for CT mentioned above are applicable to the circumstance of C-arm CBCT system since they have a close relationship.

The penalized weighted least-squares (PWLS) is a useful algorithm for restoring data corrupted with signal-dependent noise[32]. The PWLS objective function consists of two terms, the “data-fidelity term” and “penalty term” or “regularization term”. The relative importance of the two terms is controlled by a penalty/smoothing parameter. The choice of the penalty parameter determines the smoothness of the processed images. PWLS has been proved to be effective in either sinogram space[33,34] or image domain[35].

The aim of this study is to improve the quality of intra-operative CBCT images by suppressing noise and artifacts at low radiation dose in EVAR procedures, so that the denoised result is good enough for image interpretation or further processing (e.g. registration with pre-operative CT or post-operative CT). In this study, we propose an edge-preserving penalty based PWLS algorithm. The originality of the method is the design of edge-preserving penalty, which borrows from the advantage of bilateral filter. Furthermore, the proposed method works in the image domain, thus it can be applied retrospectively. Therefore, although the algorithm is proposed in the scope of intra-operative CBCT in endovascular aneurysm, it should be interesting in other applications in which low-dose CBCT is used.

The remainder of this paper is organized as follows. In Section 2, we first briefly review the conventional PWLS algorithm and then describe the proposed edge-preserving penalty based PWLS algorithm in details. The evaluation of the proposed method and denoised clinical results are described in Section 3. The discussion is in Section 4 and we conclude the paper in Section 5.

2. Materials and methods

2.1 PWLS method

The PWLS method aims to estimate a denoised image by minimizing the PWLS cost function. Mathematically, the cost function of PWLS can be written as

$$\Phi(f)=(\hat{y}-f)^T\Sigma^{-1}(\hat{y}-f)+\beta R(f) \quad (1)$$

This cost function consists of two terms, the first term is the weighted least-squares (WLS) criterion, where $\hat{y}$ represents the noisy CBCT image and f represents the ideal image to be estimated. Σ is a diagonal matrix with the ith element of estimated variance σ_i^2 at pixel i, which plays a weighting role in the WLS function. Although the noise in the reconstructed images is correlated, in this study we used a non-correlated approximation for simplicity, namely we assume that noise between pixels is uncorrelated, thus to easily get the variance σ_i^2 at every pixel. We assumed that the noise was non-stationary Gaussian distributed and used the local variance in a neighborhood to estimate the noise. Actually it is difficult to establish a noise model in the reconstructed CBCT image and Gaussian model is not the sole choice, other models would result in a change of the cost function in (1). Symbol T denotes the transpose operator. The second term $R(f)$ is the "penalty term" or "regularization term", reflecting a priori information penalizing the solution. β is the smoothing parameter which controls the strength of the penalty.

2.2 Edge-preserving penalty

There are many choices for the penalty term in (1) including smoothing and edge-preserving regularization terms, among which the common choice is the quadratic function based on Markov random fields. Generally, the quadratic smoothness penalty regularizes the sum of squared differences between the pixel and its neighbors and can be expressed as

$$R(f)=f'Rf=\frac{1}{2}\sum_i\sum_{m\in N_i}\omega_{im}(f_i-f_m)^2 \quad (2)$$

where N_i indicates the neighborhood of the pixel i and ω_{im} is the weight for neighbor pixel m. In previous applications, ω_{im} is set to 1 for the horizontal and vertical neighbors and $1/\sqrt{2}$ for the diagonal neighbors[31,36]. The weights do not include any information on intensity but are equal for neighbors of equal distance, thus leading to a blurred image. To overcome this shortcoming, several edge-preserving penalties were proposed to regularize the solution. For example, Wang[16] presented an anisotropic penalty by choosing the diffusion coefficient function to calculate the weight ω_{im}. Zhang[37] performed a similar application using the weight function in nonlocal means filtering for preserving edges. It follows that a nonlinear expression can play an important role on edge-preserving smoothing in the PWLS algorithm. The anisotropic penalty in [16] is described as follows:

$$\omega_{im}^{anisotropic}=\omega_{im}^{isotropic}\exp\left[-\left(\frac{f_i-f_m}{\delta}\right)^2\right] \quad (3)$$

$$\omega_{im}^{isotropic}=\begin{cases}1, & \text{for first-order neighbors}\\ 1/\sqrt{2}, & \text{for second-order neighbors}\end{cases} \quad (4)$$

where δ is a controlling parameter in the anisotropic diffusion coefficient function and the strength of the diffusion during each iteration is codetermined by δ and the gradient. The parameter δ can be set to a fixed value or the value at 90% of the histogram of the gradient magnitude of the image to be processed according to the study in [16]. The anisotropic diffusion applies a smaller penalty if the gradient is larger which usually occurs at edges, and vice versa.

In addition, the nonquadratic penalty is well known as its edge-preserving ability. Two representative ones are the TV (Total Variance) penalty[38] and the Huber penalty[39]. The TV penalty function has the following form:

$$TV(x)=|x| \quad (5)$$

The Huber penalty function has the following form:

$$Huber(x)=\min\{x^2,2|x|-1\} \quad (6)$$

In addition, previous studies have shown that the bilateral filtering is capable of edge-preserving smoothing[40-42]. Inspired by the bilateral filter, we herein proposed an edge-preserving penalty in which the combination of closeness function and similarity function used in the well-known bilateral filter was used to determine the weights in a neighborhood. The new $\omega_{im}^{edge-preserving}$ can be calculated as

$$\omega_{im}^{edge-preserving}=\exp(-\|i-m\|^2/2\sigma_d^2)\cdot\exp(-|f_i-f_m|^2/2\sigma_r^2) \quad (7)$$

The function is composed of two Gaussian functions including the spatial domain Gaussian function with standard deviation σ_d and the intensity domain Gaussian function with standard deviation σ_r. Parameters σ_d and σ_r respectively control the spatial weight and intensity weight. Given a fixed set of parameters $\{\sigma_d, \sigma_r\}$, the spatial domain Gaussian function gives a higher weight to pixels that are spatially close to the center pixel, and vice versa. Similarly, the intensity domain Gaussian function gives a higher weight to pixels that are similar to the center pixel in gray. In detail, in the smooth regions, a higher weight can effectively smooth the noise; while in the edge and texture regions, a small weight can well preserve the edges and textures.

σ_d is relatively insensitive to noise variance compare to σ_r, so it could be fixed in practical applications so that we need not take time to find the real optimal one. In this study, the value of σ_d is set to 2 according to experiments on CBCT data from 17 patients. σ_r changes with different slices due to the fact that the noise level varies significantly across slices in CBCT images. The noise level can be estimated using the value at 90% of the histogram of the gradient magnitude of image to be processed. Therefore, at each iteration, σ_r is set according to the histogram of the gradient magnitude of temporary image.

Several methods can be used to find the optimal solution by minimizing the PWLS cost function. In this study, we adopted the Gauss-Seidel algorithm. Therefore, the iterative formula for the solution in (1) is given by

$$f_i^{(k+1)} = \frac{y_i + \beta\sigma_i^2\left(\sum_{m\in N_i^1}\omega_{im}^{edge-preserving} f_m^{(k+1)} + \sum_{m\in N_i^2}\omega_{im}^{edge-preserving} f_m^{(k)}\right)}{1+\beta\sigma_i^2\sum_{m\in N_i}\omega_{im}^{edge-preserving}} \tag{8}$$

where N_i^1 indicates the upper and left neighbors of f_i and N_i^2 indicates the lower and right neighbors of f_i. Index *k* indicates the iteration number and the iterations can be stopped by setting a threshold according to the change of objective function or the iteration number.

2.3 CBCT acquisition

Our study was mainly based on the use of patient specific data, and this study was approved by our hospital's ethics committee. The study protocol was approved by the institutional review board. Patient informed consent was obtained for being registered anonymously in the database. The intra-operative CBCT during an EVAR usually includes pre-deployment and post-deployment CBCT. The former is related to CBCT imaging after the guidewire is introduced into the artery from the femoral artery, and the latter is related to CBCT imaging after the stentgraft is deployed. In the post-deployment CBCT, both guidewire and stentgraft can be seen.

The Siemens AXIOM Artis with Syngo DynaCT was used in the operation room and CBCT was performed on a stationary patient who was undergoing an EVAR. The C-arm CBCT system generated a complete volumetric dataset via a single 200° rotation around the patient during the 3D acquisition. Three protocols is preset in this system, they are 5sDSA protocol, 8sDSA protocol and 20sDSA protocol. Low dose intra-operative CBCT was realized using a 5sDR protocol, which has a 5-second acquisition time with the frame rate of 30f/s. Other acquisition parameters were: the distance from the X-ray source to detector is 1199 mm, the field of view (FOV) is 100 mm×100 mm, the slice thickness is 0.4804 mm, the size of one slice of the CBCT is 512×512 and pixel spacing is 0.4804 mm ×0.4804 mm. The data of two patients were used in our study, and the related scanning parameters were 91KV, 243mAs and 99KVp, 220mAs, respectively.

2.4 Image quality evaluation

The proposed denoising algorithm is evaluated using experiments on pre-deployment and post-deployment CBCT from the same patient. For quantitative analysis, we defined a local SNR to estimate the noise suppression in a region of interest (ROI) after denoising. The SNR is defined as the mean pixel value over a ROI divided by its standard deviation and indicates how the ROI is smoothed. A higher SNR indicates a better smoothing in the ROI. However, even if the image has a high SNR, it is not useful unless there is a high enough CNR to be able to distinguish among different tissues and tissue types. We used CNR to measure the contrast between a ROI and the background region. The most common definition of image contrast is:

$$C_{AB} = |\mu_A - \mu_B| \tag{9}$$

where μ_A is the mean value inside the ROI and μ_B is the mean value of the uninform background region. The CNR is defined as

$$CNR_{AB} = C_{AB}/\sigma_N = |\mu_A - \mu_B|/\sigma_n \tag{10}$$

where σ_n is the standard deviation of noise and characterized by the standard deviation of a uniform background region. It should be noted that the noise correlation was not considered in the definitions of SNR and CNR.

Another measure for in-plane spatial resolution is the MTF (Modulation Transfer Function) which is approximately obtained by using the guidewire in a pre-deployment CBCT slice. The wire was inserted into patient during the operation and is indicated

by the arrow in Fig. 1. In this study, the wire with a small diameter is approximately seen as the point source. A ROI (indicated by blue square) placed at the center of the wire was extracted and the line spread function (LSF) was then obtained by integrating the ROI in *y*-direction, finally the in-plane MTF can be obtained by calculating the Fourier transform of the normalized and zero-padded LSF.

3. Results

In this section, we present experimental results to evaluate the efficacy of the proposed method. In the proposed method, parameters σ_d and σ_r are set according to the process described in Section 2.2. Beyond that, three parameters, the smoothing parameter β, neighborhood size of N_i and iteration number *k*, affect the denoised results as well. As the image quality is affected by data acquisition protocol, in Section 3.1 and 3.2, we study the effects of changes in these parameters, to see how parameters affect the results, and what kinds of setting can give good results in the case of low dose acquisition protocol. We first discuss the effect of changes in the parameters mentioned above and then compare results from the proposed edge-preserving penalty with the isotropic penalty, TV penalty, Huber penalty and the anisotropic penalty in [16].

3.1 Effect of changes in parameter β and neighborhood size

The parameter β controls the strength of regularization and determines how the regularization item is penalized to the WLS measurement. In order to evaluate the effect of β in the proposed algorithm, we first set the neighborhood size of N_i as 3×3 and the iteration number *k*=6 with which we can get a good visual effect, and then a series of denoised images were obtained by increasing β from 10^{-6} to 10 with 10 times growth. Fig. 2 presents the denoised results under varying values of β. Fig. 2 (a) is the original slice of pre-deployment CBCT and Fig. 2 (b) shows its magnified image on bones and tissues to better illustrate noise and artifacts. We observe that noise and streak artifacts are apparent in the original image. Fig. 2 (b1)-(h1) show the magnified denoised results with different values of β, respectively. Obviously, a too small β cannot suppress noise and artifacts, whereas with a large adjustment of β ($\beta \geq 10^{-2}$), noise and artifacts are effectively removed and the results are very close in terms of vision. It seems that from Fig. 2 the effects of results are extremely similar when β equals to 10^{-2}, 10^{-1}, 1, and 10. So in our paper we set β to 10^{-2}. In addition, in the case of 5×5 neighbors, *k*=2, various results were obtained with different value of β from 10^{-6} to 10, shown in Fig. 2 (a2)-(h2). The reason that we set *k*=2 is because bones become blurred when *k* is larger.

Further evaluations using SNR and CNR measurements were used to confirm this point that β affects the result little when the other parameters are fixed. CNR in each denoised image with different β was calculated by using (9) and (10) for the selected low-contrast region indicated by the blue square in Fig. 2 (a) and the background region indicated by the white square. Fig. 3 (a) and Fig. 3 (b) depict the SNR and CNR curves with different values of β in cases of 3×3 neighbors, *k*=6, and 5×5 neighbors, *k*=2, respectively. The SNR value and CNR value in the original image are also included and indicated in red dot. It is obvious that in both cases the SNRs in all the denoised images are higher than that in the original image. When β reaches to a certain value, the SNR doesn't increase any more even if the value of β increases. It is clear that the CNR displays similar behavior with SNR.

In addition, from Fig. 3 (a), we can observe that when β is greater than a certain value, SNR in the denoised image obtained with 3×3 neighbors, *k*=6 is higher than that in the image obtained with 5×5 neighbors, *k*=2; on the contrary, it is lower than that with 5×5 neighbors, *k*=2. The two SNR curves encounter at around $\beta = 10^{-3}$. We can get similar conclusion from CNR curves in Fig. 3 (b) as well. In addition, comparing Fig. 2 (d1) with Fig. 2 (d2) ($\beta = 10^{-3}$), it seems that they have similar visions, whereas when $\beta > 10^{-3}$, images obtained in case of 3×3 neighbors, *k*=6 look better in the respect of edge preserving. Therefore, it comes to the conclusion that the proposed algorithm with combination of 3×3 neighbors and *k*=6 performs better than the combination of 5×5 neighbors and *k*=2 according to the SNR, CNR measurements and the visual effect as well.

Since SNR and CNR mainly aim at the low-contrast region, MTF evaluation in high-contrast was also performed to study the effect of the edge-preserving PWLS on spatial resolution. It's important to maintain this high-contrast MTF in order to distinctly see relevant features such as the edges of bony structures and the guidewire. The original CBCT slice shown in Fig. 1 is seen as the baseline image. Fig. 4 (a) shows MTF curves for images after denoising using the proposed method with 3×3 neighbors, *k*=6 and 5×5 neighbors, *k*=2, respectively (β=0.01). We observe that curves calculated from denoised images in both cases are close to the solid curve from the baseline image. This consequently indicates that the proposed algorithm has similar spatial resolution property with the baseline image. In other words, the edge-preserving PWLS can achieve noise reduction with good capability of preserving edges. Furthermore, the MTF curve in case of 3×3 neighbors, *k*=6 is higher than that in case of 5×5 neighbors, *k*=2, indicating that the proposed algorithm has better capability of preserving edge when neighborhood size is 3×3, *k*=6. This also confirms the conclusion that 3×3 neighbors have better performance. As a consequence, a neighborhood size of 3×3 is a better choice for practical application. Fig. 4 (b) shows the MTF curves of the denoised images obtained using the proposed PWLS

with different smoothing parameters β ranging from 10^{-6} to 10 in case of 3×3 neighbors, k=6. We observe that MTF curves are overlapped together with β increasing from 10^{-5} to 10, and very close to curves at $\beta=10^{-6}$. Fig. 4 (c) shows the corresponding MTF curves in case of 5×5 neighbors, k=2. Similarly, these curves are overlapped together. From Fig. 4 (b) and Fig. 4 (c), we therefore get the conclusion that the resolution loss will not appear even if the smoothing parameter β increases.

3.2 Effect of changes in iteration number k

In order to evaluate the effects of various combinations of iteration number k and neighborhood size in the proposed algorithm, Fig. 5 (a1)-(d1) presents the denoised results under varying values of k for a given $\beta = 0.01$ and neighborhood size of 3×3. It reveals that a small k (k =2) has small effect on noise and artifacts suppression, while a large k (k =10, 20) leads to an over-smoothed result in which bones are very blurred, especially in Fig. 5 (d1). Fig. 5 (a2)-(d2) presents the corresponding results with 5×5 neighbors. We see that the denoised image has a tradeoff between noise suppression and edge preservation at less iterations (k=2), but more and more blurred with k increases. In addition, images obtained with 5×5 neighbors are more blurred with those obtained with 3×3 neighbors under the same iteration number. The iteration number k has a strong effect on the denoised result, thus it is important to stop the iteration before the image is heavily blurred. We find that for a given β =0.01 the result has a good tradeoff between noise suppression and edge preservation with k=6 when 3×3 is selected, and k=2 when 5×5 is selected.

In fact, we need more iterations if a smaller β is selected no matter what is the neighborhood size, for example, 20 iterations is needed to achieve a tradeoff for $\beta=10^{-4}$ in the case of 3×3 neighbors. Fig. 6 depicts curves of normalized values of the objective function in (1) with different values of β for 3×3 neighbors and 5×5 neighbors, respectively. From the curves, it is clear that the objective value decreases with iterations and more slowly with a smaller β; that is, a small β corresponds to a large k and vice versa. However, it is not easy to find an optimal β with a certain criterion to stop the algorithm before the image is over-smoothed. In addition, the estimation of noise variance in (1) is less accurate in the case of 5×5 neighbors because it contains more information of edges and structures in this case. Because of this, the image is drastically smoothed after few iterations. In this study we choose β=0.01 with 3×3 neighbors taking computation time into account, and stop the algorithm according to our experiments shown in Fig. 5.

3.3 Comparison with other penalties

In this section, we compare the proposed edge-preserving penalty with the isotropic penalty, TV penalty, Huber penalty and the anisotropic penalty in [16].

The slice 169 of CBCT (as shown in Fig. 2 (a)) and the slice 19 were used to test the proposed method. Fig. 7 shows the filtered images obtained by different PWLS algorithms. Fig. 7 (a1) and Fig. 7 (a2) are the original CBCT slices, respectively. It is obvious that serious artifacts and noise exist in both slices. Fig. 7 (b1)-(f1) displays the filtered images for slice 169 obtained by the PWLS algorithms with isotropic penalty, TV penalty, Huber penalty, anisotropic penalty and the proposed edge-preserving penalty. Parameters in each PWLS algorithm were appropriately set so that the noise level in each denoised image was matched with each other. The noise level was estimated by the SNR measurement for the ROI indicated by the blue square in Fig. 2 (a). The SNR values of the corresponding ROIs in the filtered images obtained by the five methods are 52.28, 52.01, 52.33, 52.06 and 52.12, respectively. The smoothing parameter β was set to 0.078, 5.6×10^{2} in PWLS with isotropic penalty, 4.5×10^{2} in PWLS with TV penalty, 4.5×10^{2} in PWLS with Huber penalty, 0.125 in PWLS with anisotropic penalty, and 0.001 in PWLS with the proposed penalty. Similarly, the denoised results (as shown in Fig. 7 (b2)-(f2)) for slice 19 were obtained by five PWLS algorithms at a matched noise level that measured by the region indicated by the blue square in Fig. 7 (a2). We observe that the noise and artifacts in the images obtained by five PWLS algorithms are well suppressed compared with the original images. However, the edges of bone are blurred in Fig. 7 (b1) and Fig. 7 (b2), a similar blur occurs at the inserted guidewire as well, as indicated by red arrows. There is no doubt that the blurred image is caused by the isotropic weights which contain no intensity information. Seeing from Fig. 7 (c1)-(f1) and Fig. 7 (c2)-(f2), these four penalties perform well on the edges of bones and guidewire. However, for TV penalty, the staircase effect appears and the denoising capability is weak as seen in Fig. 7 (c1) and (c2). By comparison, there is no staircase effect appearing in Fig. 7 (d1)-(e1) and Fig. 7 (d2)-(e2). It seems that the Huber and anisotropic penalties yield more sharp edges of bones compared with the proposed edge-preserving penalty, but some artifacts around bones and terrible streak artifacts in low-contrast regions are not well suppressed by Huber and anisotropic penalties comparing to those by the proposed penalty, especially in Fig. 7 (d2) and (e2). The results demonstrate that the proposed edge-preserving penalty has a better capability of suppressing the streak artifacts, which may be crucial for observing guidewire and stentgraft in the application of intra-operative CBCT in endovascular aneurysm repair.

3.3.1 CNR and profile comparisons

To quantitatively compare the performances of the PWLS algorithms with different penalties, we then calculated the CNR at the matched noise level for the selected low-contrast ROI (indicated by blue square in Fig. 2(a)). Table I lists the CNR values in Fig. 7(b1)-(f1), respectively. From Table I we can see that CNR of the denoised image from the proposed edge-preserving is

higher than those from the other penalties. Fig. 8 shows the horizontal profiles through row 275 in Fig. 7(b1)-(f1). The horizontal profile is indicated by the blue line in Fig. 7(a1). Through those profiles, we can see that the proposed penalty performs better than the other penalties on smoothing in homogeneous region. These observations show that the proposed edge-preserving penalty has a better performance on streak artifacts suppression than the other penalties.

3.3.2 MTF comparison

In order to further assess the performances of different penalties, we calculated the MTFs for Fig. 1. Fig. 9 depicts the MTF curves from the five PWLS with proper parameters. Namely, parameters in each algorithm were appropriately set so that the noise level in each denoised image was matched with each other. The noise level was estimated by the SNR measurement for the ROI indicated by the red square in Fig.1. The SNR values of the corresponding ROIs in the filtered images obtained by the five methods are 29.83, 29.96, 30.58, 30.64 and 30.31, respectively. We can observe from Fig. 9 that MTF curves for the proposed edge-preserving penalty and the anisotropic penalty are very closed and higher than those from the isotropic, TV and Huber penalties. This means that the anisotropic penalty and the proposed penalty perform similarly on preserving edges and better than the other penalties at the matched noise level.

3.3.3 Clinical patient examples

Although we compared results from different methods in Fig. 7 in which only two slices were tested, we need more slices and CBCT data of different patients to demonstrate the good capability of noise suppression and edge-preserving of the proposed algorithm. CBCT data from 17 patients were tested in our study, the data includes both pre-deployment and post-deployment data, and thus a total of 34 CBCT datasets were tested. In this section, we selected pre-deployment and post-deployment CBCT data from two patients and processed these data using different PWLS algorithms. CBCT were acquired using the 5sDR protocol of the Siemens AXIOM Artis with slices of 263 and 365. Fig. 10 displays full layout results obtained by applying five penalties on the post-deployment CBCT. We observe that although the isotropic penalty suppresses much noise, the stentgraft and bones structures are blurred seriously (Fig. 10 (b)). In Fig. 10 (c)-(e), bones and stentgraft are well maintained but plenty of noise still remained, not only seen in axial view, but also in sagittal and coronal views. In contrast, the proposed algorithm has a good tradeoff between noise suppression and edge preservation in Fig. 10 (f).

Fig. 11 shows the pre-deployment CBCT of another patient. Filtered results obtained by isotropic penalty, TV penalty, Huber penalty, anisotropic penalty and the proposed edge-preserving penalty are displayed in Fig. 11 (b)-(f), respectively. Obviously, the isotropic penalty leads to an over-smoothed result with blurred bones; the TV, Huber, and anisotropic penalties performs well on preserving edges, but fails to remove artifacts; by contrast, the proposed edge-preserving penalty can effectively suppress artifacts at the same time preserve edges.

4. Discussion

Developing low-dose X-ray imaging protocols in medicine is a topical subject. In vascular diseases, the number of endovascular procedures is yearly growing, and concerns about radiation are more topical than ever. While determinist risks are finally uncommon for patients, medical staff and young surgeons especially have a lifelong X-ray exposition. Beyond reducing radiation risks of decades exposition, works dealing with low-dose X-ray imaging protocols are appropriate for optimization of the clinical use of this acquisition. Several methods have been proposed to improve the quality of CBCT images involving suppressing noise and artifacts for projections and the reconstructed images. However, edges in projections are not well defined, leading to some loss of sharpness in the reconstructions, while the spatial structures are better defined and evident in the reconstructed images. In this study, we have proposed an improved PWLS with edge-preserving penalty to reduce noise and artifacts meanwhile preserving details in CBCT images. The edge-preserving weight function in quadratic form takes both intensity similarity and spatial closeness among neighboring pixels, and performs like a bilateral filter. Thus, noise and artifacts are effectively suppressed at the same time edges are better preserved. In Section 3, we found that with a fixed iteration number the resolution loss would not appear even if the smoothing parameter β increases, while when β is fixed, the image becomes blurred as iterations progress, but this just means that β is too high. Given the computation time, the most practical approach is to only perform a few iterations coupled with a large β.

A limitation of the proposed method is that only the variance at every point in the reconstructed image is used to estimate the noise property. A more accurate way is to use the noise property of projection data, however, it requires additional calibration. Moreover, in automatic exposure control system using CBCT, the radiation dose referring to the low-dose protocol is adaptively adjusted according to the shape and weight of the patients. Thus, the noise level varies significantly for different patients and changes across slices even in one CBCT. The proposed PWLS algorithm is therefore based on the assumption that noise in CBCT is signal-dependent and estimated using the local variance of each pixel, thus forming a noise map in the proposed algorithm. However, this estimation is less accurate in case of 5×5 neighbors because the estimated noise variance not only contains information of noise and artifacts, but also useful information of edges and structures in this case. Because of this, the proposed algorithm drastically smooths the image after few iterations and we must stop it before it is converged, or the result will

be blurred. Therefore, one of our later studies is to make an accurate estimation of noise. Moreover even if the proposed method already gives significant improvement over no denoising, more sophisticated methods are possible and could be considered and tested in future work. In addition, the proposed method was only applied to each 2D slice of the 3D image, making the information from the successive slices was not concerned. However, the extension of the proposed PWLS to 3D CBCT application will take more time compare to the performance on 2D image. Considering the practical application, we processed the CBCT data slice by slice.

In this study, we also included the results obtained by the PWLS with isotropic penalty, TV penalty, Huber and the PWLS with anisotropic penalty proposed in [16]. All the experiments were performed on a clinical CBCT system with 5sDR protocol on patients, who underwent EVAR. The comparisons of profiles and CNRs demonstrate the fact that the proposed edge-preserving penalty has better ability to preserve edges and structures when reducing noise and artifacts compared with the other four penalties. For further comparison, we approximately estimate the MTF of different results from the five PWLS algorithms using the inserted guidewire. The MTF curves show that at the matched noise level the anisotropic penalty and the proposed edge-preserving penalty have similar effects on preserving edges. The anisotropic penalty generates more sharp edges in some slices; however, it is not suitable to all the slices of a CBCT, thus can be used commonly.

Our study aims to process the intra-operative CBCT at low dose so that a more accurate segment and registration, on the one hand, can be carried out, thus to guide and monitor the insertion procedure. On the other hand, a post-procedural CBCT with good noise reduction helps assessment of early complications and eliminates the time needed to transfer a patient from the angiography suite to a conventional computed tomography scanner. The proposed method has been demonstrated to be effective for all the CBCT acquisition during the operation, no matter pre-deployment or post deployment, with contrast agent or without.

Although the proposed method can reduce noise and artifacts, and be used for the improvement of low-contrast regions without degrading the spatial resolution of high-contrast regions, computational time has also to be considered. It takes about 5.5 min to process a CBCT data of 365 slices using mixed programming with MATLAB and C language under the environment that OS: 32-bit; Windows 7; CPU: Intel Core(TM) 2 Duo, 4G RAM. Nowadays, there is a trend toward the use of graphical processing unit (GPU) in order to accelerate image processing at a low cost[44-46]. Consequently, the computational time of performing the proposed method is believed to be reduced by using GPU.

5. Conclusion

In this paper, we have proposed an edge-preserving penalty based PWLS algorithm for intra-operative CBCT with low dose radiation under the assumption that the noise is non-stationary Gaussian distributed. The proposed method not only suppresses noise and artifacts, but also improves the contrast for low-contrast regions. Comparisons with results from the isotropic, TV, Huber and anisotropic penalties have shown that the proposed method has good performance for the CBCT in an EVAR procedure.

Acknowledgments

This work has been partially conducted in the experimental platform TherA-Image (Rennes, France) supported by Europe FEDER. This work has been partially supported by the French National Research Agency (ANR) in the context of the Endosim project (grant n° ANR-13-TECS-0012).

Conflict of interest statement

The authors declare no conflict of interest.

References

[1] N. S. Herana, J. K. Songa, K. Nambaa, W. Smitha, Y. Niimia, and A. Berensteina, “The utility of DynaCT in neuroendovascular procedures,” AJNR. Am. J. Neuroradiol, vol. 27, no. 2, pp. 330-332, Feb. 2006.

[2] L. Biasi, T. Ali, L. A. Arumagum, I. Loftus, R. Morgan, and M. Thompson, “Intra-operative DynaCT improves technical success of endovascular repair of abdominal aortic aneurysms,” J. Vasc. Surg., vol. 49, no. 2, pp. 288–295, Feb. 2009.

[3] L. Biasi, T. Ali, L. R. Hinchliffe, R. Morgan, I. Loftus, and M. Thompson, “Intraoperative DynaCT detection and immediate correction of a type la endoleak following endovascular repair of abdominal aortic aneurysm,” Cardiovasc. Intervent. Radiol., vol. 32, no. 3, pp. 535–538, May. 2009.

[4] M. L. Dijkstra, M. J. Eagleton, R. K. Greenberg, T. Mastracci, and A. Hernandez, “Intraoperative C-arm cone-beam computed tomography in fenestrated/branched aortic endografting,” J. Vasc. Surg., vol. 53, no. 3, pp. 583–90, Mar. 2011.

[5] P. Törnqvist, N. Dias, B. Sonesson, T. Kristmundsson, and T. Resch, “Intra-operative Cone Beam Computed Tomography can Help Avoid Reinterventions and Reduce CT Follow up after Infrarenal EVAR,” Eur. J. Vasc. Endovasc. Surg., vol. 49, no. 4, pp. 390–395, Apr. 2015.

[6] V. Tacher, M. Lin, P. Desgranges, J. F. Deux, T. Grünhagen, J. P. Becquemin, A. Luciani, A. Rahmouni, and H. Kobeiter, “Image guidance for endovascular repair of complex aortic aneurysms: comparison of two-dimensional and three-dimensional angiography and image fusion,” JVIR. vol. 24, no. 11, pp. 1698–706, Nov. 2013.

[7] H. Kobeiter, J. Nahum, and J. P. Becquemin, “Zero-contrast thoracic endovascular aortic repair using image fusion,” Circulation, vol. 124, no. 11, pp. e280-e282, Dec. 2011.

[8] A. Hertault, B. Maurel, J. Sobocinski, T. M. Gonzalez, M. L. Roux, R. Azzaoui, M. Midull, and S. Haulon, “Impact of hybrid rooms with image fusion on radiation exposure during endovascular aortic repair,” Eur. J. Vasc. Endovasc. Surg., vol. 48, no. 4, pp. 382–390, Oct. 2014.

[9] A. M. Sailer, M. W. de Haan, A. G. Peppelenbosch, M. J. Jacobs, J. E. Wildberger, and G. W. H. Schurink, “CTA with fluoroscopy image fusion guidance in endovascular complex aortic aneurysm repair,” Eur. J. Vasc. Endovasc. Surg., vol. 47, no. 4, pp. 349–356, Apr. 2014.

[10] M. M. McNally, S. T. Scali, R. J. Feezor, D. Neal, T. S. Huber, and A. W. Beck, “Three-dimensional fusion computed tomography decreases radiation exposure, procedure time, and contrast use during fenestrated endovascular aortic repair,” J. Vasc. Surg., vol. 61, no. 2, pp. 309–316, Feb. 2015.

[11] A. Kaladji, A. Dumenil, M. Castro, P. Haigron, J. F. Heautot, and S. Haulon, “Endovascular Aortic Repair Of A Post-Dissecting Thoracoabdominal Aneurysm Using Intraoperative Fusion Imaging,” J. Vasc. Surg., vol. 57, no. 4, pp. 1109-1112, Apr. 2013.

[12] A. Hertault, B. Maurel, M. Midulla, C. Bordier, L. Desponds, M. S. Kilani, J. Sobocinski, and S. Haulon, “Minimizing Radiation Exposure During Endovascular Procedures: Basic Knowledge, Literature Review, and Reporting Standards,” Eur. J. Vasc. Endovasc. Surg., vol. 50, no. 1, pp. 21–36, Jul. 2015.

[13] M. L. Kirkwood, G. M. Arbique, J. B. Build, C. Timaran, J. A. Anderson, and R. J. Valentine, “Deterministic effects after fenestrated endovascular aortic aneurysm repair,” J. Vasc. Surg., vol. 61, no. 4, pp. 902–907, Apr. 2015.

[14] M. K. Islam, T. G. Purdie, B. D. Norrlinger, H. Alasti, D. J. Moseley, M. B. Sharpe, J. H. Siewerdsen, and D. A. Jaffray, “Patient dose from kilovoltage cone beam computed tomography imaging in radiation therapy,” Med. Phys., vol. 33, no. 6, pp. 1573–1582, Jul. 2006.

[15] N. Wen, H. Guan, R. Hammoud, D. Pradhan, T. Nurushev, S. Li, and B. Movsas, “Dose delivered from Varian's CBCT to patients receiving IMRT for prostate cancer,” Phys. Med. Biol., vol. 52, no. 8, pp. 2267–2276, Apr. 2007.

[16] J. Wang, T. Li, and L. Xing, “Iterative image reconstruction for CBCT using edge-preserving prior,” Med. Phys., vol. 36, no. 1, pp. 252–260, Jan. 2009.

[17] R. C. Orth, M. J. Wallace, and M. D. Kuo, “C-arm cone-beam CT: general principles and technical considerations for use in interventional radiology,” JVIR, vol. 19, no. 6, pp. 814–820, Jun. 2008.

[18] R. D. Lee, “Common image artifacts in cone beam CT,” AADMRT Newsletter, pp. 1–7, Jul. 2008.

[19] M. Kachelrieß, O. Watzke, and W. A. Kalender, “Generalized multi-dimensional adaptive filtering for conventional and spiral single-slice, multi-slice, and cone-beam CT,” Med. Phys., vol. 28, no. 4, pp. 475–490, May. 2001.

[20] A. Manduca, L. Yu, J. D. Trzasko, N. Khaylova, J. M. Kofler, C. M. McCollough, and J. G. Fletcher, “Projection space denoising with bilateral filtering and CT noise modeling for dose reduction in CT,” Med. Phys., vol. 36, no. 11, pp. 4911–4919, Oct. 2009.

[21] L. Yu, A. Manduca, J. Trzasko, N. Khaylova, J. M. Kofler, C. H. McCollough, and J. G. Fletcher, “Sinogram smoothing with bilateral filtering for low-dose CT, ” in Proc. SPIE 6913, Medical Imaging, San Diego, CA, Feb. 2008.

[22] Z. Li, L. Yu, J. Trzasko, J. Fletcher, C. McCollough, and A. Manduca, “Adaptive nonlocal means filtering based on local noise level for CT denoising,” Med. Phys., vol. 41, no. 1, pp. 011908, Jan. 2014.

[23] Y. Chen, W. Chen, X. Yin, X. Ye, X. Bao, L. Luo, Q. Feng, Y. Li, and X. Yu, “Improving low-dose abdominal CT images by weighted intensity averaging over large-scale neighborhoods,” Eur. J. Radiol., vol. 80, no. 2, pp. e42–e49, Nov. 2011.

[24] L. Shi, Y. Chen, H. Shu, L. Luo, C. Toumoulin, and J. Coatrieux, “Low-dose CT image processing using artifact suppressed dictionary learning,” in Proc. IEEE Int, Conf. Biomed. Imag., Beijing, Apr. 2014, pp. 1127–1130.

[25] S. Ghadrdan, J. Alirezaie, J. Dillenseger, and P. Babyn, “Low-dose computed tomography image denoising based on joint wavelet and sparse representation,” in Proc. Annu. Int. Conf. IEEE Eng. Med. Biol. Soc., Aug. 2014, pp. 3325–3328.

[26] F. Yu, Y. Chen, and L. Luo, “CT image denoising based on sparse representation using global dictionary,” in Proc. 7th Int. Conf. Complex Medical Engineering, May 2013, pp. 408–411.

[27] L. Ouyang, T. Solberg, and J. Wang, “Noise reduction in low-dose cone beam CT by incorporating prior volumetric image information,” Med. Phys., vol. 39, no. 5, pp. 2569–2577, May 2012.

[28] E. Y. Sidky and X. Pan, “Image reconstruction in circular cone-beam computed tomography by constrained, total-variation minimization,” Phys. Med. Biol., vol. 53, no. 17, pp. 4777–4807, Aug. 2008.

[29] Y. Liu and Z. Gui, “A statistical iteration approach with energy minimization to sinogram noise reduction for low-dose X-ray CT,” Optik, vol.123, no. 23, pp. 2174–2178, Dec. 2012.

[30] S. Schafer, A. Wang, Y. Otake, J. W. Stayman, W. Zbijewski, G. Kleinszig, X. Xia, G. L. Gallia, and J. H. Siewerdsen, “Intraoperative imaging for patient safety and QA: detection of intracranial hemorrhage using C-arm cone-beam CT,” in Proc. SPIE 8671, Medical Imaging, Mar. 2013.

[31] J. Wang, T. Li, H. Lu, and Z. Liang, “Penalized weighted least-squares approach to sinogram noise reduction and image reconstruction for low-dose X-ray computed tomography,” IEEE Trans. Med. Imag., vol. 25, no. 10, pp. 1272–1283, Oct. 2006.

[32] A. Repetti, E. Chouzenoux, and J. C. Pesquet, “A penalized weighted least squares approach for restoring data corrupted with signal-dependent noise,” in Proc. 20th EUSIPCO, Aug. 2012, pp. 1553-1557.

[33] H. Lu, X. Li, I. T. Hsiao, and Z. G. Liang, “Analytical noise treatment for low-dose CT projection data by penalized weighted least-squares smoothing in the K-L domain,” Proc SPIE Med. Imaging. May 2002, pp. 146–152.

[34] T. Li, X. Li, J. Wang, J. Wen, H. Lu, J. Hsieh, and Z. Liang, “Nonlinear sinogram smoothing for low-dose X-ray CT,” IEEE Trans. Nucl. Sci., vol. 51, no. 5, pp. 2505–2513, Oct. 2004.

[35] K. Sauer and C. Bouman, “A Local update strategy for iterative reconstruction form projections,” IEEE Trans. Sig. Proc., vol. 41, no. 2, pp. 534–548, Feb.1993.

[36] P. Sukovic and N. H. Clinthorne, “Penalized weighted least-squares image reconstruction for dual energy X-ray transmission tomography,” IEEE Trans. Med. Imag., vol. 19, no. 11, pp. 1075–1081, Nov. 2000.

[37] Q. Zhang, Y. Liu, H. Shu, and Z. Gui, “Application of regularized maximum likelihood algorithm in PET image reconstruction combined with nonlocal fuzzy anisotropic diffusion,” Optik, vol. 124, no. 20, pp. 4561–4565, Oct. 2013.

[38] R. I. Boţ, and T. Hein, “Iterative regularization with a general penalty term-theory and application to L-1 and TV regularization,” Inverse Problems, vol. 28, no. 10, pp. 2635-2668, Oct. 2012.

[39] J. A. Fessler and A. O. Hero, “Penalized maximum-likelihood image reconstruction using space-alternating generalized EM algorithms,” IEEE Trans. Image Process., vol. 4, no. 10, pp. 1417-1429, Oct. 1995.

[40] B. Zhang and J. P. Allebach, “Adaptive bilateral filter for sharpness enhancement and noise removal,” IEEE Trans. Image Process., vol. 17, no. 5, pp. 664–678, May. 2008.

[41] W. Alexander, “Adaptive bilateral filtering of image signals using local phase characteristics,” Sig. Process., vol. 88, no. 6, pp. 1615–1619, Jun. 2008.

[42] N. Anantrasirichai, L. Nicholson, J. E. Morgan, I. Erchovay, and A. Achim, “Adaptive-weighted bilateral filtering for optical coherence tomography,” in proc., IEEE Int. Conf. image process., Melbourne, VIC, Sept. 2013, pp. 1110 –1114.

[43] B. Goossens, H. Luong, J. Aelterman, A. Pižurica, and W. Philips, ”A GPU-accelerated real-time NLMeans algorithm for denoising color video sequences,” in Proc. 12th Int. Conf. Advanced concepts for intelligent vision systems, Springer Berlin Heidelberg, Jan. 2010, pp. 46-57.

[44] M. G. McGaffin and J. A. Fessler, “Edge-preserving image denoising via group coordinate descent on the GPU,” IEEE Trans. Image Process., vol. 24, no. 4, pp. 1273-1281, Apr. 2015.

[45] B. Dolwithayakul, C. Chantrapomchai, and N. Chumchob, “GPU-based total variation image restoration using Sliding Window Gauss-Seidel algorithm,” In Proc. 2011 International Symposium on Intelligent Signal Processing and Communication Systems (ISPACS), Dec. 2011, pp. 1–6.

[46] F. P. X. Fontes, G. A. Barroso, P. Coupé, and P. Hellier, “Real time ultrasound image denoising,” J. Real-Time Image Process., vol. 6, no. 1, pp. 15-22, Mar. 2011.

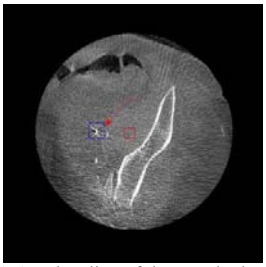

FIG. 1. The slice of the pre-deployment CBCT with the blue square selected to calculate the MTF. Display window is [-1024 HU, 1476 HU].

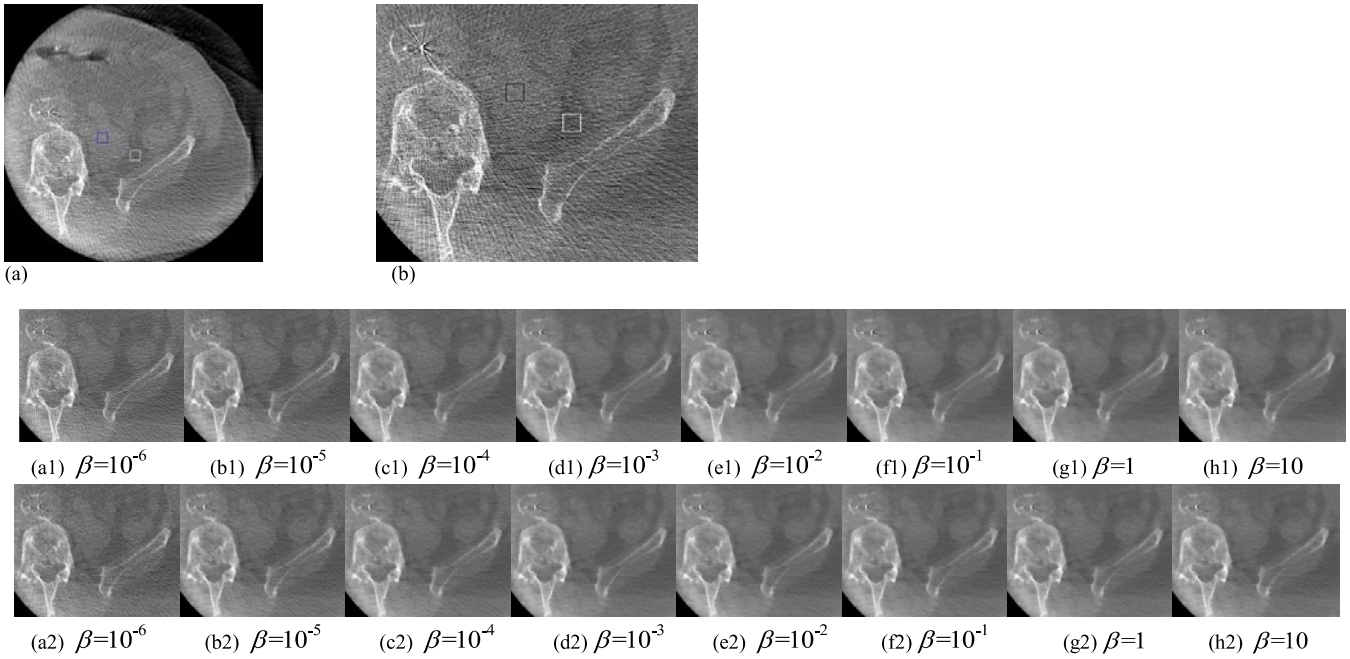

FIG. 2. Images of CBCT slice: (a) the original image, (a1)-(h1) denoised images with different β in case of 3×3 neighbors, k=6, (a2)-(h2) denoised images with different β in case of 5×5 neighbors, k=2. The blue square and white square in (a) indicate the low-contrast ROI and the background region, respectively. Display window: [-1024 HU, 1476 HU].

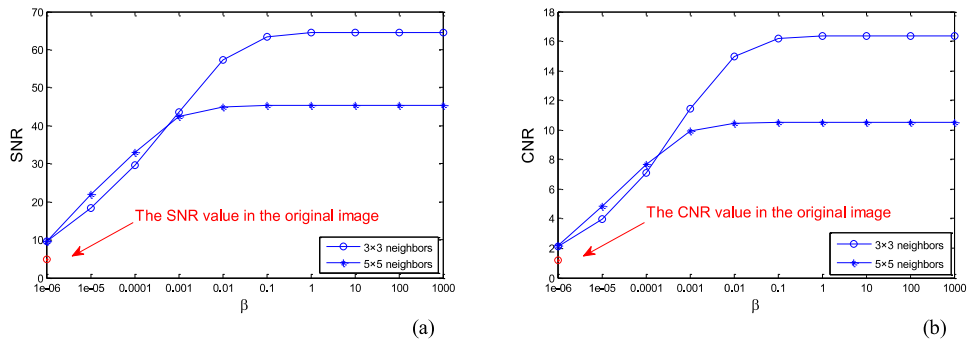

(a) (b)

FIG. 3. SNR and CNR curves with different β in case of 3×3 neighbors, k=6 and 5×5 neighbors, k=2, respectively. (a) SNR curves, (b) CNR curves.

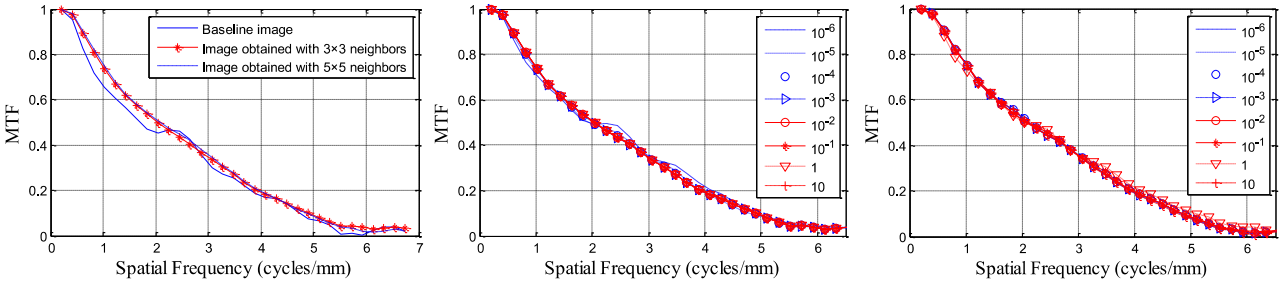

FIG. 4. Comparison of MTF curves. (a) MTF curves from the baseline and denoised images in case of 3×3 neighbors, k=6 and 5×5 neighbors, k=2 (β =0.01), (b) MTF curves of denoised images from the proposed algorithm with different values of β (3×3 neighbors, k=6), (c) MTF curves of denoised images from the proposed algorithm with different values of β (5×5 neighbors, k=2).

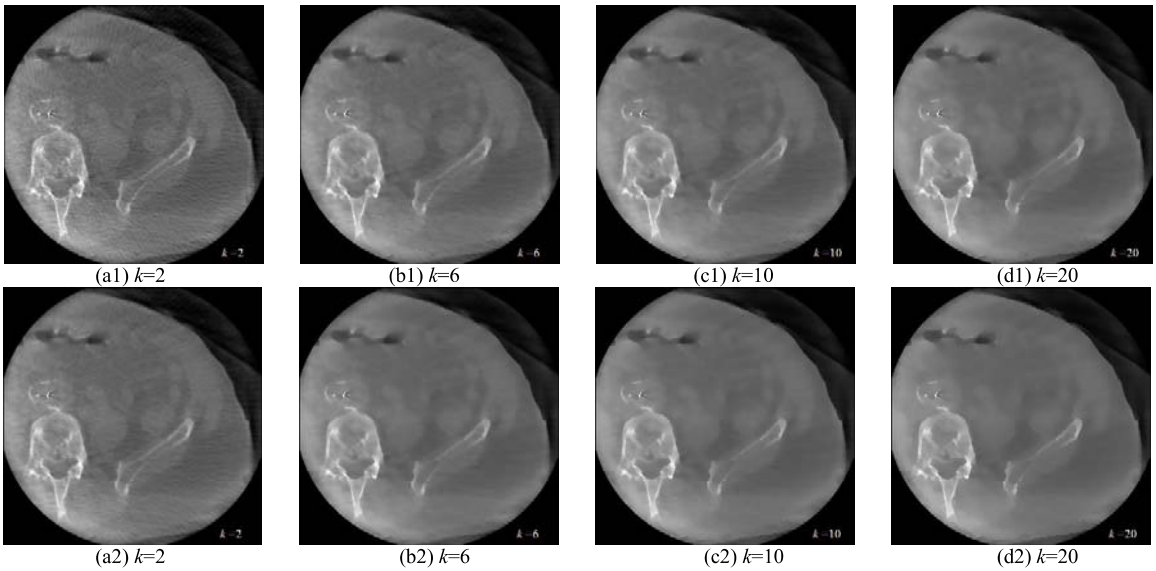

FIG. 5. Denoised results under varying iteration number k: (a1)-(d1) show images obtained with 3×3 neighbors and (a1)-(d2) show images obtained with 5×5 neighbors. (β =0.01 in each case)

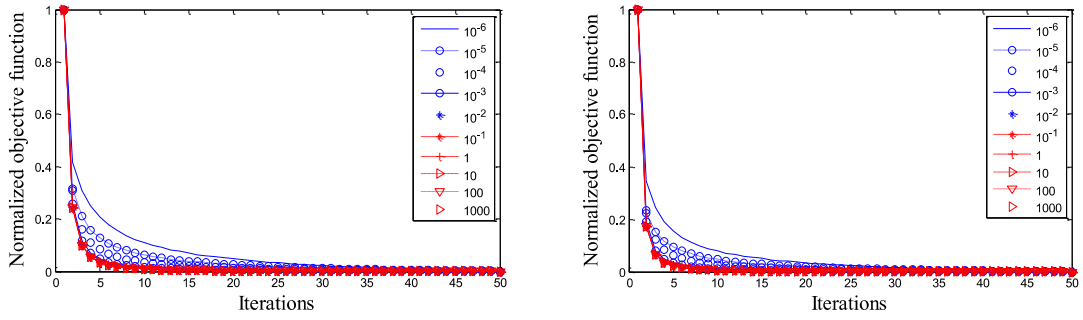

FIG.6. The curves of normalized objective function with different values of β . (a) 3×3 neighbors, (b) 5×5 neighbors.

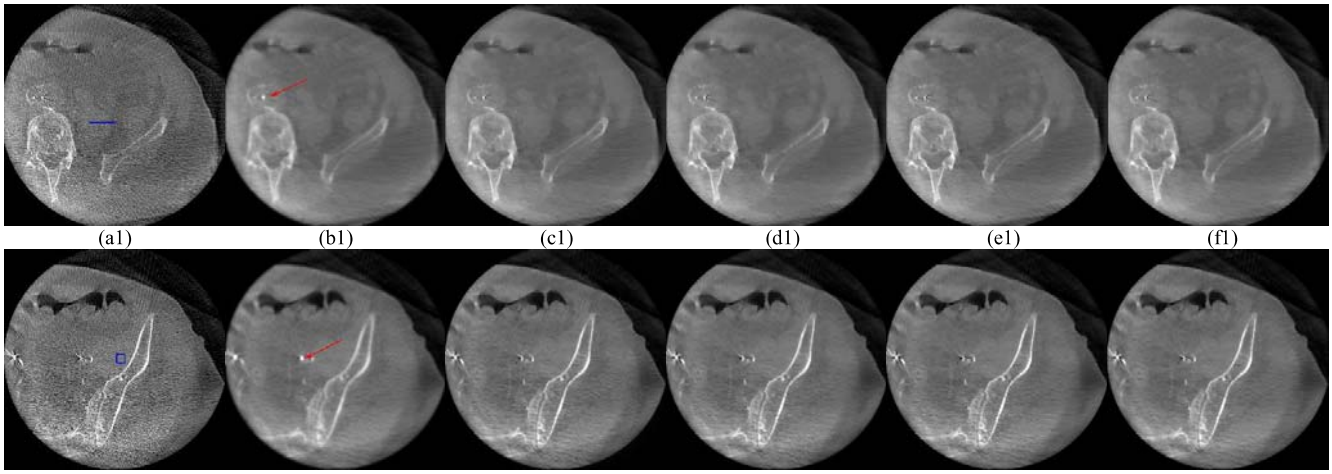

FIG. 7. CBCT slices of the abdominal vasculature: (a1) slice 169 of CBCT; (b1)-(f1) filtered CBCT slice obtained by PWLS algorithms with isotropic penalty, TV penalty, Huber penalty, anisotropic penalty and the proposed edge-preserving penalty, respectively. (a2) slice 19 of CBCT; (b2)-(d2) filtered CBCT slice obtained by PWLS algorithms with isotropic penalty, TV penalty, Huber penalty, anisotropic penalty and the proposed edge-preserving penalty, respectively. Display window: [-1024 HU, 1976 HU].

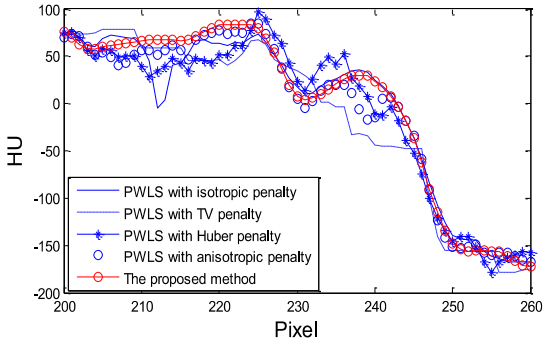

FIG.8. Horizontal profile through row 275 in Fig. 7(b1)-(f1).

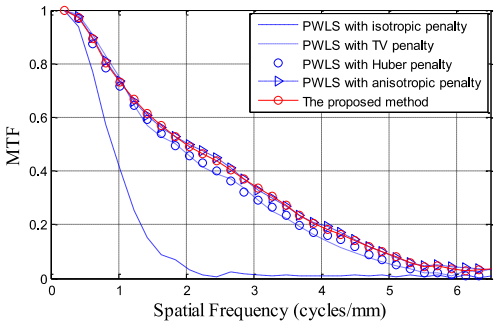

FIG.9. MTF curves of the denoised images obtained using different algorithms

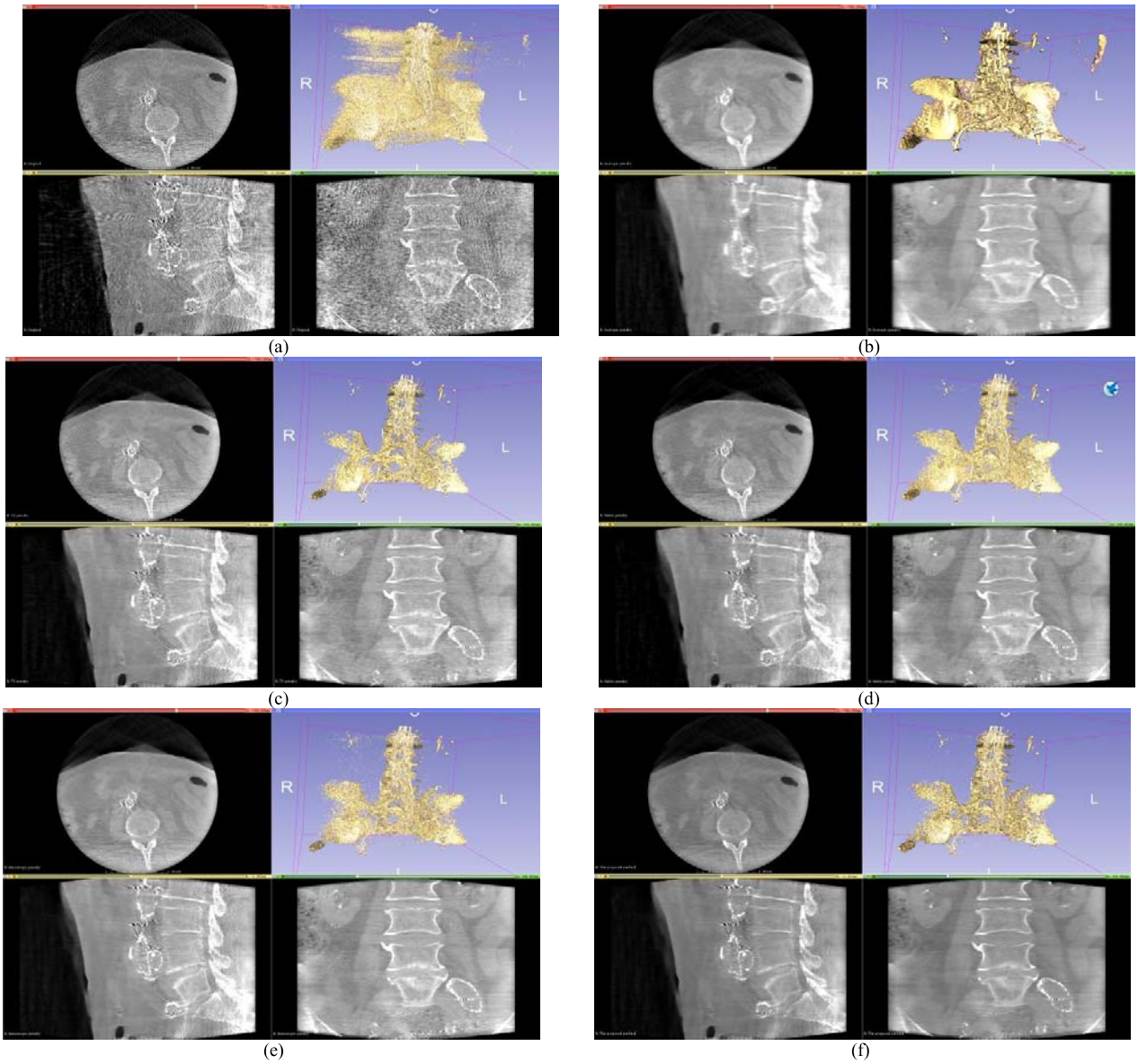

FIG.10. Post-deployment CBCT: (a) original CBCT, (b) result from the isotropic penalty, (c) result from the TV penalty, (d) result from the Huber penalty, (e) result from the anisotropic penalty, (f) result from the proposed edge-preserving penalty.

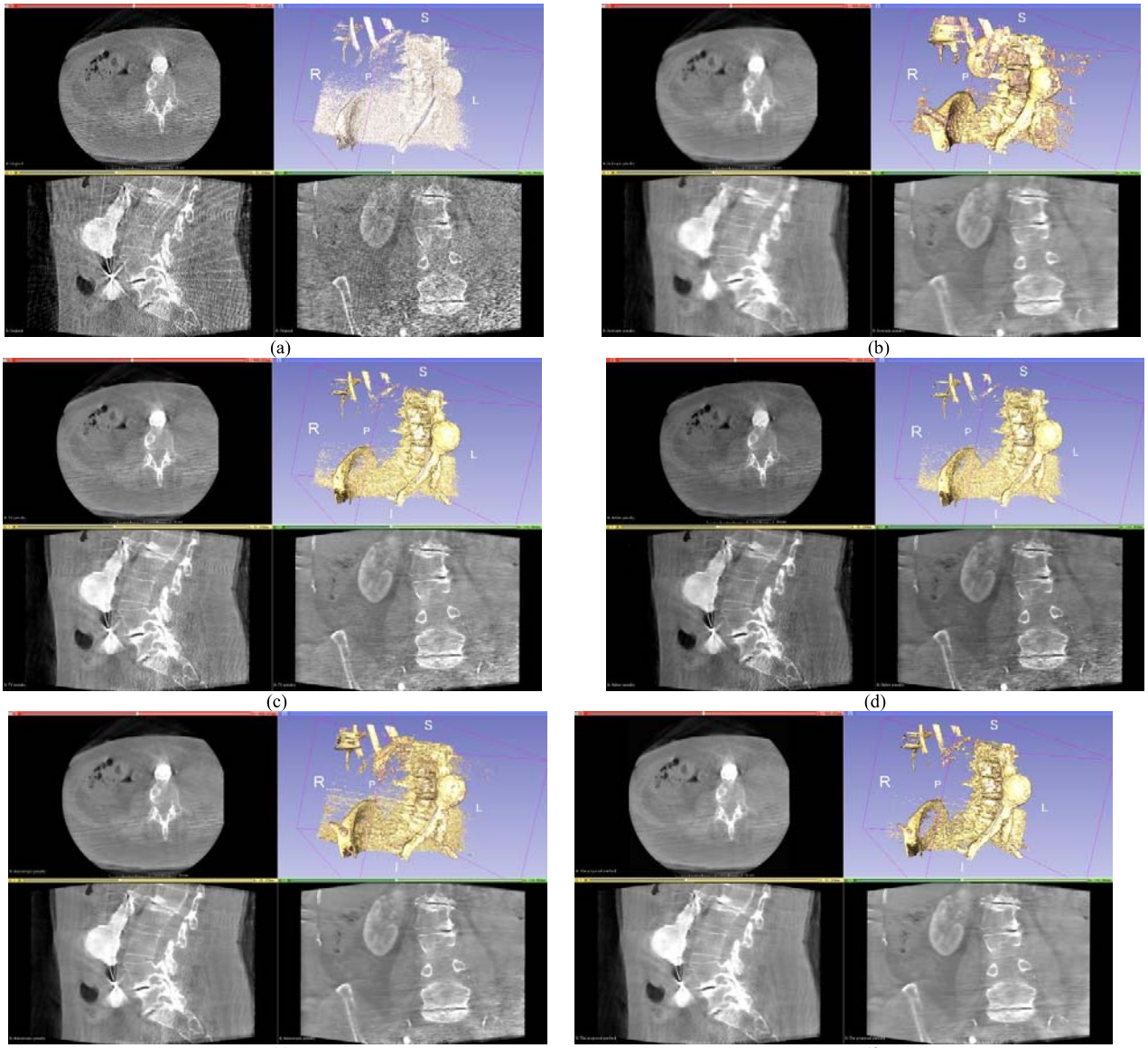

FIG.11. Pre-deployment CBCT: (a) original CBCT, (b) result from the isotropic penalty, (c) result from the TV penalty, (d) result from the Huber penalty, (e) result from the anisotropic penalty, (f) result from the proposed edge-preserving penalty.

TABLE I CNRs of the low-contrast ROI in Fig. 2 (a)

	Isotropic	TV	Huber	Anisotropic	Our penalty
CNR	13.28	12.27	11.47	12.23	13.71